

1-2008

The Identification and Verification of Hazardous Convective Cells Over Oceans Using Visible and Infrared Satellite Observations


Michael F. Donovan
Massachusetts Institute of Technology

Earle R. Williams
Massachusetts Institute of Technology

Cathy Kessinger
National Center for Atmospheric Research

Gary Blackburn
National Center for Atmospheric Research

Follow this and additional works at: <https://commons.erau.edu/publication>

Paul H. Herzegh
 <https://commons.erau.edu/publication>

Scholarly Commons Citation

Donovan, M. F., Williams, E. R., Kessinger, C., Blackburn, G., Herzegh, P. H., Bankert, R. L., Miller, S., & Mosher, F. R. (2008). The Identification and Verification of Hazardous Convective Cells Over Oceans Using Visible and Infrared Satellite Observations. *Journal of Applied Meteorology and Climatology*, 47(1). <https://doi.org/10.1175/2007JAMC1471.1>

© Copyright 2008 American Meteorological Society (AMS). Permission to use figures, tables, and brief excerpts from this work in scientific and educational works is hereby granted provided that the source is acknowledged. Any use of material in this work that is determined to be "fair use" under Section 107 of the U.S. Copyright Act September 2010 Page 2 or that satisfies the conditions specified in Section 108 of the U.S. Copyright Act (17 USC §108, as revised by P.L. 94-553) does not require the AMS's permission. Republication, systematic reproduction, posting in electronic form, such as on a web site or in a searchable database, or other uses of this material, except as exempted by the above statement, requires written permission or a license from the AMS. Additional details are provided in the AMS Copyright Policy, available on the AMS Web site located at (<https://www.ametsoc.org/>) or from the AMS at 617-227-2425 or copyrights@ametsoc.org.

This Article is brought to you for free and open access by Scholarly Commons. It has been accepted for inclusion in Publications by an authorized administrator of Scholarly Commons. For more information, please contact commons@erau.edu.

Authors

Michael F. Donovan, Earle R. Williams, Cathy Kessinger, Gary Blackburn, Paul H. Herzegh, Richard L. Bankert, Steve Miller, and Frederick R. Mosher

The Identification and Verification of Hazardous Convective Cells over Oceans Using Visible and Infrared Satellite Observations

MICHAEL F. DONOVAN AND EARLE R. WILLIAMS

Massachusetts Institute of Technology Lincoln Laboratory, Lexington, Massachusetts

CATHY KESSINGER, GARY BLACKBURN, AND PAUL H. HERZEGH

National Center for Atmospheric Research, Boulder, Colorado

RICHARD L. BANKERT AND STEVE MILLER

Naval Research Laboratory, Monterey, California

FREDERICK R. MOSHER

Applied Aviation Sciences, Embry-Riddle Aeronautical University, Daytona Beach, Florida

(Manuscript received 11 April 2006, in final form 16 April 2007)

ABSTRACT

Three algorithms based on geostationary visible and infrared (IR) observations are used to identify convective cells that do (or may) present a hazard to aviation over the oceans. The performance of these algorithms in detecting potentially hazardous cells is determined through verification with Tropical Rainfall Measuring Mission (TRMM) satellite observations of lightning and radar reflectivity, which provide internal information about the convective cells. The probability of detection of hazardous cells using the satellite algorithms can exceed 90% when lightning is used as a criterion for hazard, but the false-alarm ratio with all three algorithms is consistently large (~40%), thereby exaggerating the presence of hazardous conditions. This shortcoming results in part from the algorithms' dependence upon visible and IR observations, and can be traced to the widespread prevalence of deep cumulonimbi with weak updrafts but without lightning over tropical oceans, whose origin is attributed to significant entrainment during ascent.

1. Introduction

Continental convection hazardous to aviation has received much attention in numerous field programs over several decades, beginning with the Thunderstorm Project (Byers and Braham 1949). This pioneering study called early attention to the thunderstorm as the most hazardous convective form. This and subsequent investigations have relied heavily on aircraft, radar, and lightning observations to effectively probe the internal dynamic, microphysical, and electrical structure of thunderstorms. The updraft is a key internal variable in its influence on many aviation hazards (turbulence, ic-

ing, hail, and lightning). These internal measurements are generally augmented with satellite observations—an important surveillance tool, but one that reveals only the exterior characteristics of clouds (e.g., IR cloud temperature, cloud height), owing to the opaque nature of convective clouds in the visible and infrared region.

The present study shifts the focus in hazardous weather from land to ocean, where conditions are notably more benign (Takahashi 1978; Petersen et al. 1996, 1999; Williams and Stanfill 2002; Zipser 2003; Cecil et al. 2005; Ushio et al. 2005), but data are much more limited. The challenge undertaken here is the remote identification of hazardous oceanic convective cells, but without the critical benefit of routine surveillance by radar and lightning detection systems, which provide crucial information on the structure and pro-

Corresponding author address: Michael F. Donovan, MIT Lincoln Laboratory, 244 Wood Street, Lexington, MA 02420-9185.
E-mail: miked@ll.mit.edu

cesses interior to the cells. The mainstay of oceanic weather (OW) surveillance is the international fleet of geostationary satellites that operate in the visible and infrared. In three separate intercomparison studies, we examine three recently developed convective diagnostic algorithms that rely upon geostationary data to meet operational needs for detection of hazardous cells. The verification of convection and its hazard potential is achieved through analysis of simultaneous observations of convective cell interiors (radar reflectivity, lightning) obtained by the National Aeronautics and Space Administration (NASA) Tropical Rainfall Measuring Mission (TRMM) satellite in Low Earth Orbit (LEO). The three algorithms evaluated here were developed by Naval Research Laboratory (NRL), National Center for Atmospheric Research (NCAR), and Aviation Weather Center (AWC) under funding by the Aviation Weather Research Program (AWRP) of the Federal Aviation Administration (FAA).

A long-recognized contrast between continental and oceanic convection lies in the nature of the underlying surface. A water surface resists heating by sunlight relative to land, because the sunlight is absorbed over greater depth in the ocean and because of the greater heat capacity of ocean water and its tendency to mix with deeper water. This land–ocean contrast affects the cloud-base height and the updraft speed at cloud base (Williams and Stanfill 2002). But the existence of updraft is a basic ingredient of an electrification process that appears to be the same for land and ocean (Petersen et al. 2005). As an example in the present context, Takahashi (1978) has documented tall oceanic clouds with low lightning activity, but with electrical structure and electrically charged graupel particles similar to continental storms. The presence of tall clouds with weak updrafts is a basic finding in the present study.

The present study is not the first of its kind, and the interest in oceanic convection is on the rise as intercontinental routes expand. Work by Mahoney et al. (2000) and Martin et al. (2008) has also been concerned with the scoring and validation of one of three algorithms under consideration here (AWC).

2. Satellite-based detection algorithms

Three algorithms for convective diagnosis have been implemented for operational trials by the AWRP Oceanic Weather Product Development Team (OWPDT). Each uses data from the Geostationary Operational Environmental Satellites (GOES) and is designed to distinguish benign cloud regions from deep convection that is potentially hazardous to aviation.

a. Cloud Top Height (CTOP) product

The objective of the Cloud Top Height (CTOP) product is to determine and display the heights of clouds. Originally developed by NRL (Miller et al. 2005, unpublished manuscript) and later reimplemented by NCAR for OWPDT use, the product indicates the presence of deep convection and other cloud features over a range of flight-level altitudes. The product is currently scheduled to become operational in 2008 and thereafter serve to advise pilots, dispatchers, and air traffic controllers on the presence of deep convection and other cloud types over land and ocean on a global scale (Herzogh et al. 2002). The product is currently generated in real time over land and ocean for three large domains: the central Pacific Ocean, the northern Pacific Ocean and the Gulf of Mexico. Coverage for the North Atlantic Ocean is scheduled to begin in 2007–08.

Production of the CTOP product begins with projection of the 11- μm IR window channel satellite brightness temperature data onto an equidistant cylindrical latitude–longitude grid. Over the Pacific Ocean within $\pm 35^\circ$ of latitude, data from both the *GOES-9* and *GOES-10* satellites are required to complete this coverage and were used in these studies. The CTOP algorithm will utilize data from the Japanese geostationary Multifunction Transport Satellite (MTSAT) upon completion of algorithm modifications. In regions where the GOES satellites overlap each other, the data are mosaicked with no parallax correction. Because of variations in satellite scanning strategies, update rates, and data latency associated with ingest, the Pacific domain CTOP product is computed every 20 min using all data that are available. If no new data are received within the 20-min update period, the previous data are used. Data from the *GOES-12* are used to cover the Gulf of Mexico domain with an update interval of 30 min. No mosaic is required for the latter domain.

The next step is to acquire sounding data from the National Centers for Environmental Prediction (NCEP) Global Forecast System (GFS) numerical model. The model data, at a $1^\circ \times 1^\circ$ horizontal resolution, are transferred to the same map projection as the IR temperature grid. For each satellite grid cell, the corresponding column of model temperature and pressure data was located using a nearest-neighbor approach, and was then used to identify the two model layers that bound the satellite brightness temperature. Data are interpolated to obtain the geopotential height for the satellite data and the corresponding GFS pressure via the hypsometric equation interpolation. Finally, the pressure (hPa) is converted to flight-level (kft) altitudes using a

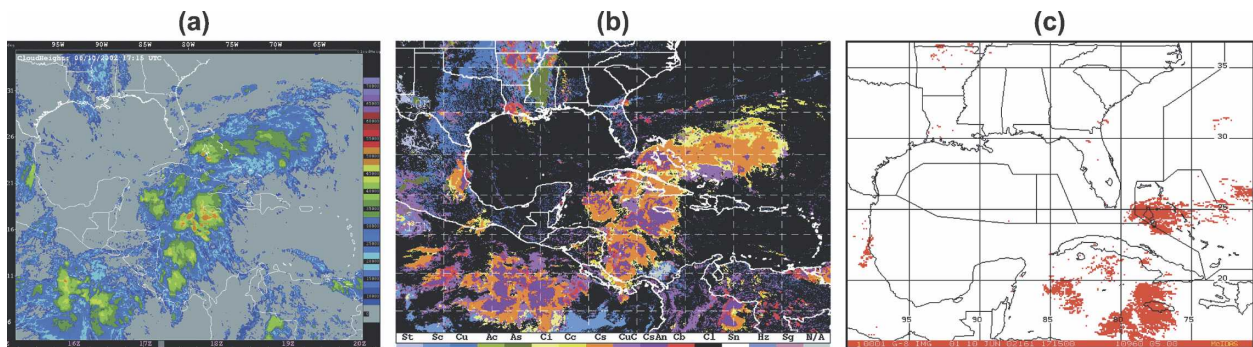


FIG. 1. Illustration of convection diagnoses from the (a) CTOP, (b) CC, and (c) GCD algorithms observed over the Gulf of Mexico on 10 Jun 2002 at 1715 UTC. Deep convective clouds that are potentially hazardous to aviation are denoted as cloud heights ≥ 40 kft (12.2 km) (light green), cloud class types CsAn (magenta) and Cb (red), and red detections by the CTOP, CC, and GCD algorithms, respectively.

standard atmosphere to be consistent with aviation usage. Figure 1a shows an example of the CTOP product over the Gulf of Mexico where numerous convective cells have developed from south of Cuba to the Bahamas Islands. Warmer colors represent higher cloud tops. Deep convection indicated by contour levels greater than 40 kft (12.2 km) indicates potential aviation hazards.

b. Cloud Classification (CC) product

The NRL Cloud Classification (CC) algorithm (Tag et al. 2000) is another product that is used by the OWPDT to assist in the accurate detection of deep convective clouds. The CC product classifies satellite imagery into several cloud types or layers and has been optimized to provide coverage over the western Atlantic Ocean, continental United States, and eastern Pacific Ocean.

Training sets were based on all combinations of *GOES-8/-10*, day–night (as defined by the solar zenith angle), and land–ocean samples where collective agreement of the cloud-type classification was reached among three independent experts interpreting the samples. These data were drawn from thousands of $16 \text{ km} \times 16 \text{ km}$ (day) and $32 \text{ km} \times 32 \text{ km}$ (night) samples created from *GOES-8* and *GOES-10* scenes. All *GOES-8* samples were adjusted to better emulate the *GOES-12* data that now cover the former Atlantic domain of *GOES-8*. Adjustments include a visible channel bias correction to compensate for the stronger visible signal from the *GOES-12* sensor and removal of the *GOES-8* $12\text{-}\mu\text{m}$ channel training data.

Over 100 characteristic features were computed or extracted from each of the training samples using all GOES Imager channels during the day and all but the visible channel at night. The difference in resolution of

the water vapor channels between *GOES-8* and *GOES-12* had little or no affect on the features used and no modification was necessary. The feature set is subsequently reduced by applying a feature selection algorithm (Bankert and Aha 1996) to the training data for each classifier resulting in 10–15 features that maximize classification accuracy. Various classes are identified (i.e., cirrus, stratus, etc., for daytime; and thin–thick high, low, etc., for nighttime). There is no class for nimbostratus clouds. These clouds are classified as either cirrostratus (Cs) or cumulonimbus (Cb) if the spatial distribution of cloud-top data exhibits textural features. The main interests in the present study are the Cb and cirrostratus associated with deep convection (CsAn) classes (for daytime classifications) and the deep convection (DC) class (for nighttime classifications).

The CC algorithm is a 1-nearest-neighbor classifier with each sample within an image given the same class as the training sample it most closely resembles (minimum Euclidean distance) within the feature space. All satellite pixels within the sample are assigned the same class. Satellite sample boxes overlap each other such that pixels are classified four times except near the image edges. The final classification of the pixel becomes the simple majority. An example of a daytime classification image over the southern United States and neighboring oceanic regions is shown in Fig. 1b. The daytime classifier delineates among several cloud types, as is evident between the high thin cirrus (Ci) and cirrostratus (Cs) clouds and the vertically developed clouds (CsAn and Cb) located south and northeast of Cuba.

c. Global Convective Diagnostic (GCD)

A third experimental algorithm designed to detect deep convection and thunderstorms was developed at

the AWC (Mosher 2002). The algorithm computes the satellite temperature difference between the 6.7- μm water vapor channel and the 11- μm infrared channel to identify deep convection. The diagnostic product is produced globally since all geostationary satellites contain these two channels.

The premise behind the algorithm is that the 11- and 6.7- μm infrared radiance from a cloud will be the same if the cloud is optically thick and the water vapor above the cloud is negligible. This condition of negligible water vapor implies that the top of the thick cloud is near the tropopause. Thunderstorms are the most common optically thick clouds near the tropopause. The difference between the two channels can be used to identify these optically thick clouds at high altitude. Temperature differences between the two channels greater than 1° can be caused by thin clouds allowing radiation from below, or by water vapor above the clouds. For thin clouds the blackbody emissivity is less than unity, allowing radiation to come through the cloud as well as to be emitted by the cloud top. For the 11- μm channel the radiation from below originates near the ground or from lower clouds. For the 6.7- μm channel the radiation from below originates from upper-level water vapor below the cloud. Hence a large temperature difference is expected for thin clouds. Likewise, if water vapor lies above the cloud, the 6.7- μm radiation will originate from this water vapor while the 11- μm radiation will come from the cloud. Again, a large temperature difference is expected for clouds below the level of the moisture. Large temperature differences can be used to eliminate thin cirrus clouds, thunderstorm anvil edges, and lower clouds. The algorithm eliminates any cloud regions in which the infrared temperature is higher than the water vapor temperature by 1°C or more.

In some circumstances cirrus cloud formation not associated with thunderstorms can be mistakenly detected by the algorithm (i.e., wind motions near jet streams and within midlatitude storm development). In practice, the application of the GFS model 4-layer Lifted Index (LI) stability product has shown promise in eliminating these instances. The GCD algorithm utilizes the LI product to eliminate all areas where the LI values are greater than 1°C, indicating stable atmospheric conditions.

Merging techniques are applied to reconcile areas of overlapping satellite coverage and time skew among the suite of geostationary satellite samples. The final product is a composite diagnostic that highlights as “convective” all areas not eliminated by the stability filter. The spatial and temporal resolutions of the product are 10 km and 30 min, respectively. Figure 1c illus-

trates the GCD product (thunderstorms are depicted with a red color) over the Gulf of Mexico and Caribbean Sea.

3. Algorithm verification: Use of TRMM products

Orbiting the earth at a 35° inclination angle, the TRMM satellite was designed to procure information on the distribution of rainfall and heat exchange in the tropics. Observations from its Visible and Infrared Radiometer System (VIRS), precipitation radar (PR), and Lightning Imaging Sensor (LIS) provide a three-dimensional view of the internal structure of deep convection not presently available from any geostationary satellite, and thereby yielding an unprecedented opportunity for evaluation of the OW diagnostic products. The coupling of lightning and rainfall observations provides a better understanding of the relationship between lightning and precipitation and the often-pronounced differences between maritime and continental cumulonimbus clouds.

The VIRS instrument is a cross-track scanning radiometer measuring scene radiance in five channels and is similar to the Advanced Very High Resolution Radiometer (AVHRR) aboard a National Oceanic and Atmospheric Administration (NOAA) spacecraft (Kummerow et al. 1998). The track width during the period of the intercomparisons was approximately 830 km. The footprint resolution is ~ 3 km at nadir and increases toward the swath edges. The visible and infrared channels were used in the intercomparisons to link observed convective events to the PR data and to the three geosynchronous satellite-based detection algorithms. TRMM version 5A data products were used in all intercomparisons.

An integrated perspective of continental convection points to the central role of the updraft in affecting aviation hazard. Physical bases for correlated relationships between updraft and turbulence intensity (Pinsky and Khain 2002), updraft and icing/hail (Williams 2001), and updraft and lightning activity (Williams 1985; Baker et al. 1995; Boccippio 2002) are now reasonably well established. Unfortunately, despite its central role, the updraft remains an elusive variable, even over continents where Doppler radar measurements are numerous. The vertical profile of radar reflectivity, a far more accessible internal observation, is often used as a surrogate for updraft (Williams et al. 1992; Petersen and Rutledge 2001; Ushio et al. 2005; Cecil et al. 2005). This practice is continued in the present context.

The PR instrument is capable of measuring the three-dimensional rainfall distribution over the land and oceans. The swath width of the radar is approximately

247 km with a horizontal resolution slightly coarser than 5 km at nadir, and the vertical resolution is 0.25 km. The observable range of the radar extends from the near surface to an 18-km altitude. The TRMM 1C21 “normal sample” product with no attenuation correction was used in the analyses. Of great importance to these studies is the reflectivity observed at higher altitudes (above the freezing level and throughout the mixed-phase region), which is the weakly attenuated portion of the cloud. The vertical resolution of the radar is excellent for documenting individual cumulonimbus clouds, but the horizontal resolution is less than ideal given that the diameters of reflectivity cores within such clouds are often less than 5 km.

The LIS is an optical imager (Christian et al. 2003) that searches for transient pulses (intracloud and cloud-to-ground lightning) that rise above the radiance of the background scene. The optical detector has individual pixel resolutions from 3 to 6 km and a total field of view of $550 \times 550 \text{ km}^2$. The LIS, in its nominal 100-min LEO, typically observes a point on the earth’s surface for a maximum view time of 90 s and can estimate the flash rate of most storms down to $0.3\text{--}0.5 \text{ flash min}^{-1}$ (Williams et al. 2000). The elemental LIS data are grouped to correspond to physical features such as thunderstorms, flashes, and strokes. The *area* and *flash* groups (Boccippio et al. 1998) were extracted from the LIS database and used here. Areas represent regions that contain one or more flashes and correspond to individual thunderstorm cells. Flashes represent the locations of observed pulses close to each other in space and time, that is, the physical lightning flash.

Another TRMM product (2A23) used during the third intercomparison is the rain-type classification generated from the PR qualitative algorithm (Awaka et al. 1998). The objectives of this algorithm are to detect the radar bright band, classify the rain type, and detect warm rain. Rain types are in three categories: stratiform, convective, or “other,” and are used as an additional metric for characterizing deep convective clouds with potential hazard to aviation.

4. Important terminology used within studies

In the following sections that describe each intercomparison study, *hazardous cells* and *hazardous convection* both refer to *cumulonimbus clouds without lightning* (CWL) that pose a potential hazard to aviation or as *thunderclouds* (TRW), cumulonimbus clouds accompanied by lightning and increased hazard. In the second and third intercomparisons, these terms are defined further by verifying in the TRMM data that the cell contained any combination of lightning, radar reflectiv-

ity $\geq 30 \text{ dBZ}$ at 5-km altitude or convective rain. All references to *cell*, *convective cell*, *deep convection*, and *deep convective cloud* represent a vertically developed cloud identified in the TRMM and geostationary satellite-based products that are potentially hazardous under the criteria mentioned above. The choice of a height threshold (5 km) rather than a temperature threshold is mostly a matter of convenience in working with the radar observations, justified on the basis that the TRMM observations are at low latitude ($<35^\circ$) where consistent height–temperature relationships are upheld. The selection of a 5-km threshold in altitude departs from other studies also concerned with lightning activity (Shackford 1960; Williams and Lhermitte 1983; Larsen and Stansbury 1974; Marshall and Radhakant 1978; Zipser and Lutz 1994; Nesbitt et al. 2000; Cecil et al. 2005; Petersen et al. 2005) because the goal here was different. We sought a conservative threshold for “hazardous cell” rather than a lightning surrogate per se.

5. Intercomparison studies

The domains under study in each of the three intercomparisons varied because of seasonal changes in the occurrence of deep convection. The first comparison took place on 10 June 2002 during the late morning to midafternoon hours, local time, when the TRMM satellite passed over the Caribbean, Gulf of Mexico, and south-central United States. The 10 June date was selected on short notice when deep oceanic and continental air mass TRW were expected in the area. The test domain ($15^\circ\text{--}35^\circ\text{N}$ latitude and $75^\circ\text{--}105^\circ\text{W}$ longitude) is shown in blue in Fig. 2.

Because of the limited number of cells (32) analyzed in the first intercomparison, a longer period of study and a larger domain were chosen for the second exercise. The comparison took place during the daylight hours from 26 to 31 March 2003. Two regions were evaluated. One area was centered over northwestern South America ($10^\circ\text{N}\text{--}20^\circ\text{S}$, $50^\circ\text{--}80^\circ\text{W}$) where diurnal air mass TRW were expected to be numerous. The other area was in the central Pacific Ocean ($0^\circ\text{--}20^\circ\text{N}$, $120^\circ\text{--}150^\circ\text{W}$) covering a portion of the ITCZ where maritime convection was expected to be prevalent. The two regions of interest are shown in Fig. 2 as green rectangles. The analysis times were restricted to daylight hours because at that time the NRL CC was unable to classify clouds at night.

A third intercomparison was planned to analyze additional maritime cells and to evaluate the capabilities and readiness of the individual diagnostic algorithms in another climatological region. This intercomparison

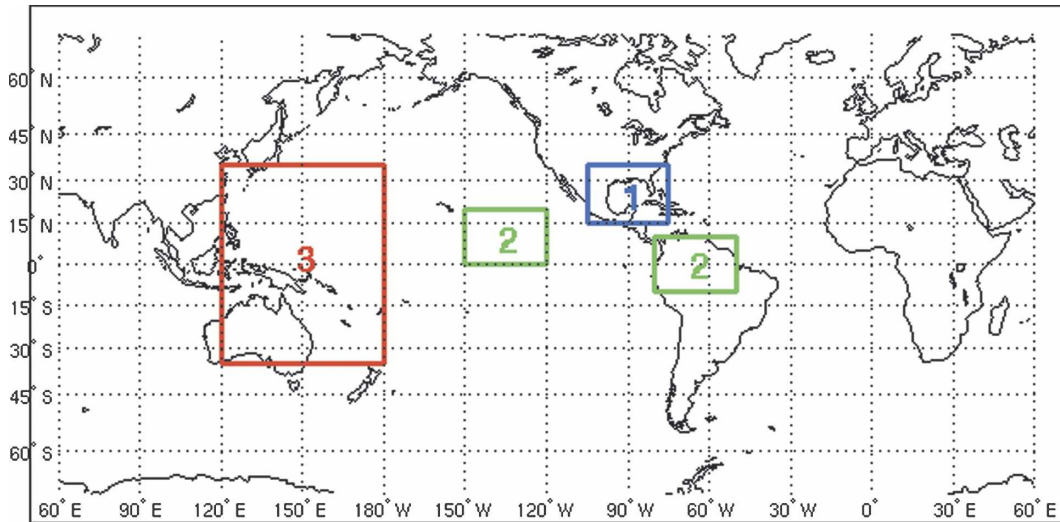


FIG. 2. Global map with each intercomparison region of interest outlined. The first, second, and third intercomparison areas studied are shown as a blue, green, and red rectangle, respectively.

was conducted over a much larger area (red rectangle in Fig. 2) in the western Pacific Ocean (35°S – 35°N , 120°E – 180°). This area was chosen to capture several types of convection, such as cold frontal systems in the central Pacific, tropical cyclone development within the ITCZ, and summer convection over Australia and Indonesia. Beginning on 4 February 2004, the OW algorithms were run daily, day and night, at 3-h intervals beginning at 0225 UTC to coincide with the full-disk scans of the *GOES-9* satellite. A nighttime classifier was developed by NRL prior to the analysis, and the spatial resolution of the GCD product was increased to 4 km, in agreement with the other diagnostic products.

In each intercomparison, all OW products and TRMM data were mapped to a common 4-km grid to assure proper spatial alignment.

a. First intercomparison: 10 June 2002

A total of 32 convective cells were identified in three TRMM orbits that intersected the Gulf of Mexico region. In this intercomparison, we define a match as any cell observed in the TRMM and geostationary satellite-based products where the two data sources were coincident within a 20-min time window. Cells were selected based on a visual inspection of the VIRS data to identify any large cloudy region (area $>700\text{ km}^2$) with high reflectance (radiance $\geq 18\,000\text{ mW cm}^{-2}\text{ }\mu\text{m}^{-1}\text{ sr}^{-1}$) and a low cloud-top temperature ($\leq 230^{\circ}\text{ K}$). The convective cells were sorted into two categories, as TRW confirmed by the LIS or as CWL. The OW products were then studied to determine their ability to detect both types of cells. The objective of the product

evaluation was to determine how each algorithm performs in detecting TRW, a known hazard to aviation, and deep CWL that are believed to be hazardous, but at a level that is currently unknown.

Of the 32 convective cells identified, 16 were categorized as TRW and 16 as more benign CWL. The OW algorithms were each scored by noting whether or not two or more detection points (pixels) matched the cloudy area for the cell of interest. Because of temporal differences, the detection signatures are not expected to exactly overlap the corresponding TRMM features, thus the percentage of overlap was not considered in the evaluation. While the algorithms do not distinguish between cells on the basis of lightning, they do identify the location of convective features. For the CTOP product, convection is identified as cloud tops $\geq 40\text{ kft}$ (12.2 km). The CC product associates convection with the cumulonimbus or cirrostratus cloud that frequently accompanies deep convection. For the GCD product, satellite channel differences (water vapor channel – infrared channel) $\geq -1^{\circ}\text{C}$ coupled with an LI $\leq 1^{\circ}\text{C}$ indicates deep convection.

Probability of detection (POD) and false-alarm ratios (FAR) results for each algorithm are shown in Table 1. The POD for each category type is the ratio of the number of TRW (CWL) detected as convection by the algorithm to the total number of TRW (CWL) verified by TRMM. The FAR is the number of incorrect detections issued to the total number of TRW and CWL. The performance statistics of the CTOP algorithm at lower height thresholds are also provided in the table. The CC and GCD algorithms were able to

TABLE 1. POD with fraction correct (in parentheses) and FAR with fraction of false alarms (in parentheses) for three satellite diagnostic products applied to detection of two types of cloud categories, TRW and CWL, during the first satellite intercomparison on 10 Jun 2002.

| Satellite product | POD | | FAR |
|---------------------------------|--------------|--------------|-------------|
| | TRW | CWL | |
| CC | 1.0 (16/16) | 0.94 (15/16) | 0.13 (4/31) |
| GCD | 0.88 (14/16) | 0.94 (15/16) | 0.03 (1/29) |
| CTOP \geq 40 kft (12.2 km) | 0.38 (6/16) | 0.56 (9/16) | 0.0 (0/15) |
| CTOP \geq 35 kft (10.7 km) | 0.69 (11/16) | 0.81 (13/16) | 0.0 (0/24) |
| CTOP \geq 30 kft (9.1 km) | 1.0 (16/16) | 1.0 (16/16) | 0.16 (5/32) |

detect greater than 85% of both cloud types, while the CTOP algorithm performance was substantially lower, detecting only 38% and 56% of the TRW and CWL, respectively. The cloud heights of all the convective cells exceeded 30 kft (9.1 km), suggesting that the CTOP product would have benefited through use of a lower threshold setting. However, the usefulness of these results is inadequate because of the limited sophistication of the product evaluation and utilization of the TRMM data in this study.

While the TRMM radar data provide a means of observing the internal structure of a convective cell, this information was not used as a metric for categorizing cloud types in this intercomparison. However, these data were useful for generating vertical reflectivity profiles for 17 of the cells located in the narrow PR swaths and determining any characteristic differences in structure between the 7 TRW and 10 deep CWL. Profiles were created by obtaining the maximum reflectivity value within a 14-km radius (to guarantee access to the maximum value at each level) from the cloud center at each 250-m interval from near surface up to the 15-km altitude. Reflectivity profiles for a TRW and CWL observed in the Gulf of Mexico are shown in Fig. 3. The TRW profile shows larger reflectivity values extending to higher altitudes, suggesting a vigorous updraft, whereas the largest reflectivity values in the CWL profile are limited to the lower altitudes, indicating weaker updrafts. Consistent with earlier studies (Nesbitt et al. 2000; Petersen and Rutledge 2001) similar features were observed in the other seven maritime profiles.

The inherent difficulty that each diagnostic algorithm faces in determining the hazard level of a convective cell is that, while the cloud type or cloud-top height may be reasonably identified, none is able to determine how strong or turbulent the updraft may be inside the cloud. Generally, as a cloud deepens, so does its maximum

updraft speed (Williams 1985) and peak lightning flash rate (Williams 2001). The problem over the oceans is that deep convection is typically less energetic and less hazardous than over land (LeMone and Zipser 1980; Jorgensen and LeMone 1989; Williams and Stanfill 2002). Visible imagery of the TRMM overpass in a portion of the western Atlantic and Gulf of Mexico in Fig. 4 illustrates the difficulty in diagnosing hazardous oceanic convection. Based on general experience with convection over land, nearly all of the large, ominous oceanic cells suggest a real hazard to aviation, yet only four of them (shown with circles) contain lightning.

b. Second intercomparison: 26–31 March 2003

The second intercomparison was conducted over 6 days in late March 2003 and significantly extended the database of cases. This analysis was also restricted to the daylight (local afternoon) hours, and a match refers to any cell identified in the TRMM and geostationary satellite products at locations where the data were coincident within a 30-min time window. Analysis for the geostationary satellite products was performed for a total of 14 Pacific and 8 South American TRMM overpasses. Unlike the first intercomparison where the solar zenith angle was very small, some of the March cases occurred when the solar zenith angle was $>82^\circ$ (as the day is transitioning to night). Since the darkening of the satellite imagery that results can provide erroneous data leading to misclassifications of cloud type, the NRL algorithm was unable to perform cloud classifications under these circumstances.

Because the goal of the OWPDT is to develop a real-time diagnosis of the locations of convective-related hazards, the TRMM data are quite useful to differentiate between hazardous and nonhazardous cells and to evaluate the ability of each diagnostic to make such inferences. Consequently, and in contrast with the first study, both radar and lightning observations were used to distinguish a hazardous cell from a nonhazardous cell. The TRMM LIS and PR data were examined for the presence of lightning or reflectivity values ≥ 30 dBZ at an altitude of 5 km. If one or both observations were made, the cell was considered hazardous and the OW diagnostic products were scored accordingly. This reflectivity criterion was chosen because significant reflectivity found in the mixed-phase portion of a cloud is necessary for electrical charge separation and the formation of lightning (Larsen and Stansbury 1974; Marshall and Radhakant 1978; Ushio et al. 2005; Cecil et al. 2005) and could be used as a precursor to ensuing hazardous conditions to aviation. Such enhanced reflectivity also indicates a strong updraft within the cloud and

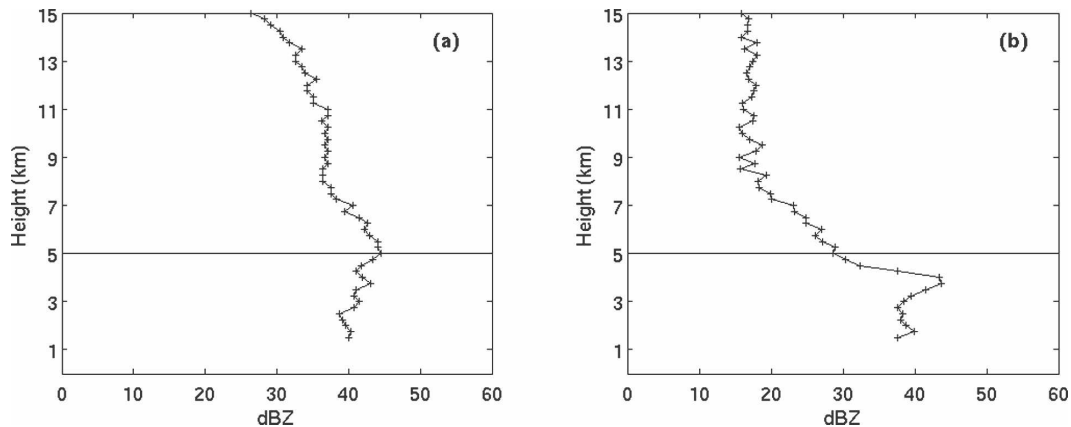


FIG. 3. Reflectivity profiles of convective cells observed by the TRMM PR over the Gulf of Mexico on 10 Jun 2002 for a (a) TRW and (b) CWL. The horizontal line at the 5-km altitude in both panels represents the approximate freezing level in tropical regions.

could lead to more turbulent conditions aloft. Outside the narrower PR swath of the TRMM orbit, the products were evaluated only if the cells contained lightning so as not to penalize the algorithms for making false detections where no underlying radar data were available. Cells were selected in a manner similar to the first intercomparison.

An example of the scoring methodology for two cells is shown in Fig. 5 and the corresponding reflectivity profiles are shown in Fig. 6. Within the VIRS visible imagery (Fig. 5a), any cloud area was considered for analysis if it exceeded the same spatial and low (i.e., cold) cloud-top temperature (IR image not shown) thresholds used in the first intercomparison. In this example, cell A, although spatially small, was characterized as hazardous because the reflectivity at 5 km was 45 dBZ (Fig. 6a) and lightning was detected. All three OW products correctly detected this cell. Cell B is significantly larger but was not considered hazardous because the reflectivity at 5 km was only 23 dBZ (Fig. 6b) and no lightning was observed. The CC algorithm correctly did not classify this cloudy area in the deep convection class, whereas the GCD and CTOP algorithms both falsely indicate this cell to be hazardous by issuing detections and a maximum cloud top of 42 kft (12.8 km), respectively.

All TRMM overpasses intersecting each domain of interest during the local afternoon hours were examined. In the South American sector, 117 hazardous cells were observed over land but only 20 hazardous cells were observed over the ocean following the criteria stipulated above. Evaluation statistics for the OW products were tabulated and categorized to show detection performance over land and ocean. The results are provided in Table 2. The scoring metrics are POD,

FAR, and critical success index (CSI). In this study, the POD is the ratio of the number of detected hazardous cells verified by TRMM (detections) to the total number of hazardous cells identified by TRMM. The FAR is the ratio of the number of detections not verified by TRMM (false alarms) to the total number of detections issued. The CSI is the ratio of the number of detections to the sum of detections, misses (failure to detect), and false alarms. The results in Table 2 show the CC detected 98% and 100% of all land and ocean hazardous cells, respectively. The GCD detected greater than 75% of all the land and ocean cells while the CTOP algorithm detected only 50% of the ocean cells using a cloud-top height threshold of 40 kft (12.2 km). The FAR among the algorithms was 14%–17% for all land cells but increased to 46% for the CC and 30% for the GCD over the ocean. With respect to CSI, the CC outperformed the other algorithms for the land cells because of fewer missed detections, but the scores were similar for the ocean cells. Employing lower height thresholds in the CTOP algorithm such as 30 (9.1 km) and 35 kft (10.7 km) yielded much higher POD rates and fewer missed detections, but with an undesirable increase in the FAR.

Despite the small number of hazardous cells (20) observed over the ocean, results from this study have yielded some significant results. While performance differences exist among the OW algorithms, each has shown a similar skill at identifying convection over land and ocean. However, the outstanding result of this study is that all algorithms tend to overestimate the presence of (presumed hazardous) maritime convection resulting in higher FARs. Consistent with numerous previous studies, the reflectivity profiles (not shown) indicate the oceanic cells are weakly developed in the

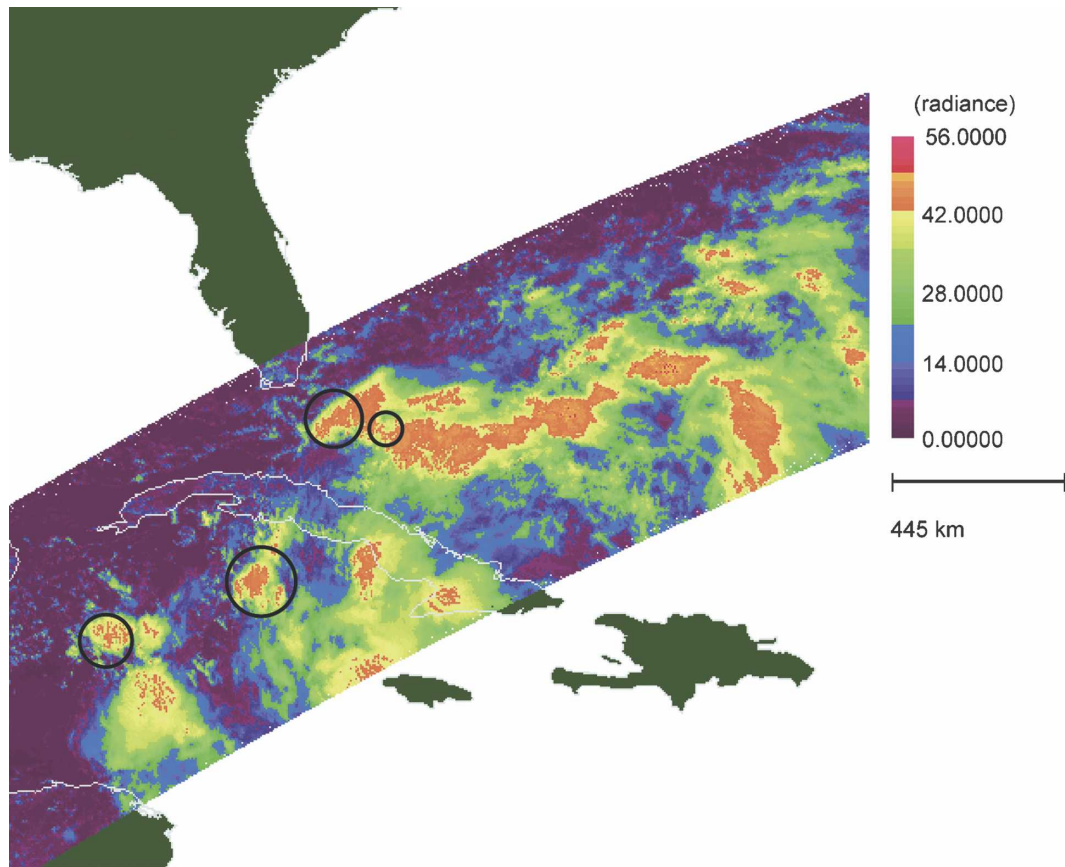


FIG. 4. Visible imagery observed by TRMM taken at 1522 UTC on 10 Jun 2002. Warmer (oranges–reds) colors denote clouds that are more reflective. Units for radiance: $\text{mW cm}^{-2} \mu\text{m}^{-1} \text{sr}^{-1}$. While most regions with high cloud tops appear hazardous to aviation, only four cells contain lightning (enclosed by circles). Image acquired from the TRMM Science Data and Information System (TSDIS) visualization software tool Orbit Viewer.

mixed-phase region of the cloud, despite the presence of high (>10 km) cloud tops.

c. Third intercomparison: 4 February–31 March 2004

Unlike the first two intercomparisons, the spatial area chosen for the third intercomparison is large enough to coincide with several TRMM overpasses each day. Products were generated at 3-h intervals beginning at 0225 UTC each day to coincide with the update rate of the *GOES-9* full-disk satellite scans and to accommodate potential limitations in processing power, disk space storage, and latencies in real-time data acquisition. In contrast with the first two intercomparisons, all OW products were evaluated both during the day and at night because of NRL's recent development of a nighttime CC algorithm. The spatial resolution of the GCD product was also improved from 10 to 4 km.

Special consideration was given to the temporal matching of the TRMM and geostationary satellite product datasets given the very large domain of the test. By knowing the start time and the elapsed time required to complete the full disk images at the selected time intervals, it was possible to estimate the time of day for a given cell in the geostationary data given its latitudinal location. The OW product data were evaluated in regions where the approximate time of day matched the time-registered TRMM data to within 15 min. All other regions within the data grids that were not time coincident were excluded from evaluation. The domain size, frequency of TRMM overpasses, and length of study were all factors in reducing the time matching requirement from previous intercomparison studies.

The scoring methodology was similar to that in the second intercomparison, that is estimating the degree of hazard of each cell using TRMM LIS and PR data for verification. However, a third criterion for hazard

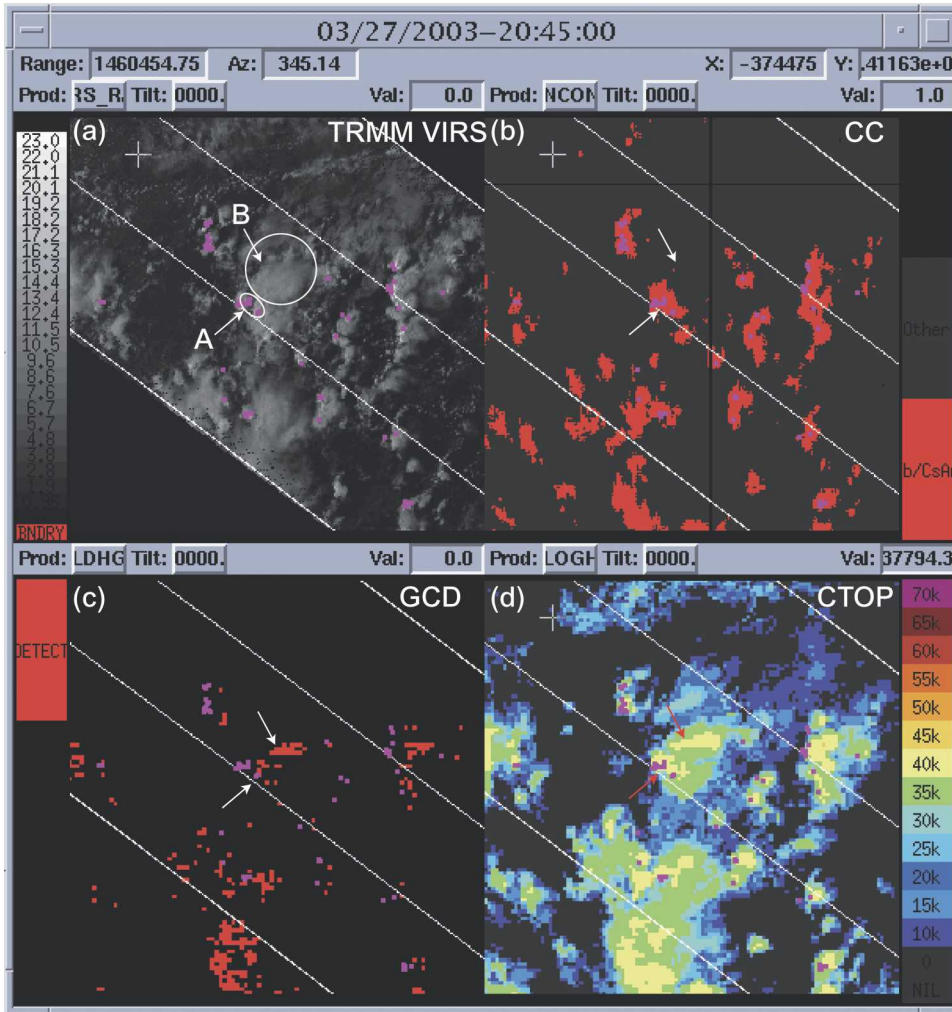


FIG. 5. Four-panel analysis display showing (a) TRMM visible imagery, (b) CC detections of the cumulonimbus and cirrostratus associated with deep convection classes, (c) GCD detections of satellite channel temperature differences $\geq -1^{\circ}\text{C}$, and (d) CTOP heights contoured in 5-kft (1.5-km) intervals. The magenta dots represent lightning flashes observed by LIS. The two parallel outer and inner lines represent the VIRS and PR swath edges, respectively. Two cells of interest (A and B) are denoted with white ovals in (a).

was added, namely the NASA method for classifying convective rain (the TRMM Qualitative Product). This rain product employs a vertical profile and horizontal pattern method (Steiner et al. 1995) to distinguish between stratiform and convective rain systems. It was decided that a small region (<10 pixels) classified as convective rain detections alone would not be classified as hazardous unless it was accompanied by lightning or significant upper-level reflectivity. Convective rain detections ≥ 10 pixels were classified as hazardous cells.

Furthermore, the convection evaluated by each diagnostic product was sorted independently into two convective regimes, “maritime” or “continental,” distinguished on the basis of fractional area of coverage of

radar reflectivity ≥ 20 dBZ at the 5-km altitude. This decision was based on earlier ground-based radar studies in tropical Australia (Williams et al. 1992), showing substantial differences in the fractional area of radar echo coverage between true continental and maritime regimes. The fractional area is the ratio of the number of pixels exceeding 20 dBZ at the 5-km altitude to the total number of pixels within a bounding box that has a width and length equal to the PR swath width (~ 247 km) and is centered on the cell of interest. As shown by Williams et al. (1992) and more recently by Nesbitt et al. (2000) and Toracinta et al. (2002), a cell exhibits maritime characteristics (large cloudy area with high cloud tops and little or no lightning) if the fractional

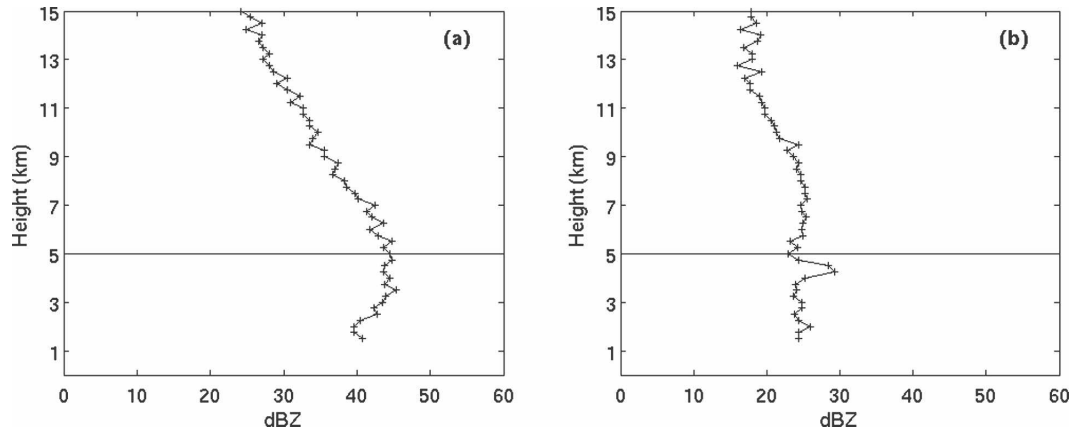


FIG. 6. Reflectivity profiles of two convective cells deemed to be (a) hazardous and (b) nonhazardous based on the criterion that the cell must contain lightning and/or measured reflectivities ≥ 30 dBZ at the 5-km altitude (horizontal line). The profile in (a) (refer to cell A in Fig. 5) meets the reflectivity criterion (45 dBZ) and has lightning associated with it. The profile in (b) (refer to cell B in Fig. 5) does not contain lightning and has weak reflectivity at 5 km (23 dBZ).

area with radar reflectivity exceeding some threshold is large. A histogram distribution of the fractional areas computed for all hazardous cells identified in the TRMM radar data (583) is provided in Fig. 7. It is clear that a high percentage of cases exhibit small fractional areas ($<10\%$) and, by inference, continental characteristics. A dividing line of 9% was arbitrarily selected as the value that roughly split the total population equally. Several cell centers located near the PR swath edges did not have as large an area from which to collect reflectivity data. The fractional area computation for these cells may yield results not representative of the actual storm status, but the occurrence was low and the overall impact on the analysis negligible.

One concern raised by a reviewer over the selection of this metric for distinguishing continental and maritime convection is that oceanic mesoscale convective systems (MCSs) might also pass the maritime test and thereby influence these results. A recent study by Nesbitt et al. (2006) indicates MCSs in larger numbers over ocean than previous estimates.

An illustration of the analysis display used for identifying common convective features in the various satellite datasets is provided in Fig. 8. The evaluation was restricted to cells located within the PR swath (denoted as the region inside the two parallel lines) and those cells that contained lightning located outside the radar swath and inside the VIRS swath. A composite of the

TABLE 2. Detection performance statistics for the three satellite products during the second intercomparison. Performance results are separated between (top) land and (bottom) ocean. The scoring metrics from left to right are as follows: Hits (number correct), misses (failure to detect), false alarms (incorrect detections), bad (product not available), detect (hits + false alarms), POD, FAR, and CSI.

| South American sector (117 hazardous cells over land) | | | | | | | | |
|---|------|--------|--------------|-----|--------|------|------|------|
| Satellite product | Hits | Misses | False alarms | Bad | Detect | POD | FAR | CSI |
| CC | 102 | 2 | 17 | 13 | 119 | 0.98 | 0.14 | 0.84 |
| GCD | 89 | 28 | 16 | 0 | 105 | 0.76 | 0.15 | 0.67 |
| CTOP ≥ 40 kft | 88 | 28 | 18 | 1 | 106 | 0.76 | 0.17 | 0.66 |
| CTOP ≥ 35 kft | 110 | 6 | 21 | 1 | 131 | 0.95 | 0.16 | 0.80 |
| CTOP ≥ 30 kft | 112 | 4 | 21 | 1 | 133 | 0.97 | 0.16 | 0.82 |
| Pacific sector (20 hazardous cells over ocean) | | | | | | | | |
| Satellite product | Hits | Misses | False alarms | Bad | Detect | POD | FAR | CSI |
| CC | 20 | 0 | 17 | 0 | 37 | 1.00 | 0.46 | 0.54 |
| GCD | 16 | 4 | 7 | 0 | 23 | 0.80 | 0.30 | 0.59 |
| CTOP ≥ 40 kft | 8 | 8 | 0 | 4 | 8 | 0.50 | 0.00 | 0.50 |
| CTOP ≥ 35 kft | 15 | 1 | 8 | 4 | 23 | 0.94 | 0.35 | 0.63 |
| CTOP ≥ 30 kft | 16 | 0 | 15 | 4 | 31 | 1.00 | 0.48 | 0.52 |

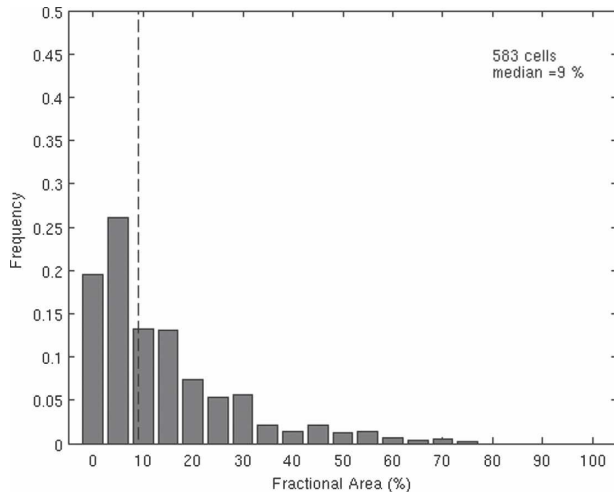


FIG. 7. Frequency distribution histogram of the fractional area of radar reflectivity ≥ 20 dBZ at the approximate freezing level (5 km) for all hazardous cells within the TRMM PR swath. The dashed vertical line represents the median of the sample (9%) and was chosen to distinguish continental (left of line) from maritime (right of line) style convective cells.

TRMM products indicating which cells contain hazardous signatures is shown in Fig. 8e. The fractional area used to distinguish between continental and maritime style cells, binned at 10% intervals, is shown in Fig. 8f.

Within the 2-month period studied, 649 cells were deemed hazardous following the criteria discussed above. Performance statistics of the OW products were compiled and are illustrated in Fig. 9. All cells containing lightning and located outside the PR swath (66) were included in the evaluation results. The CC algorithm POD performance was 78% but was also the most aggressive in overdetecting the presence of hazardous convection with a FAR of 34%. The CTOP algorithm (using a 40-kft or 12.2-km threshold) performance for POD and FAR was 63% and 21%, respectively. Again, similar to the previous studies, lowering the cloud-top height threshold from 40 kft (12.2 km) to 30 kft (9.1 km) would have raised the POD by 28% with only a modest increase (7%) in the FAR (not shown in Fig. 9). The GCD algorithm was the most conservative in the number of detections issued (more than 50% fewer detections than CC and CTOP). Fewer detections led to the lowest FAR (12%) but also resulted in a low POD (37%). The GCD results indicate that the temperature difference threshold and/or the stability index filter were too stringent. In regards to overall performance, the CSI of the CC and CTOP algorithms were similar at 55% and nearly a 20% improvement over the GCD.

The scoring statistics were broken down further into each algorithm's ability to detect hazardous cells over the ocean or land, during the day or at night, and whether they exhibited maritime or continental characteristics based on the fractional area test. Results for each category are shown in Fig. 10. The statistics show a slight performance improvement at identifying the cells (POD) observed over land from those observed over the ocean (Figs. 10a,b). This result is consistent with the second intercomparison. When comparing individual performance, the CTOP (using a 40-kft or 12.2-km threshold) and CC algorithms show marginally better performance with the cells over land than over the ocean (8% CSI increase) and both show a similar trend in overestimating the convection hazard over the ocean than over land (8% and 11% increase in FAR, respectively). Further review of the CTOP detections over the ocean shows that many of the cloud-top heights of the missed cells were in the 34–38-kft (10.4–11.6-km) range. The GCD algorithm showed little difference in performance for land and ocean cells. However, there was more variability in the temperature channel differences for the missed cells over ocean than over land.

For both land and ocean cells, the statistics also reveal that all algorithms perform markedly better at identifying the cells classified as maritime (i.e., cells that are accompanied with a large well-developed cloud mass with a significant spatial distribution of reflectivities in the mixed-phase region) over cells classified as continental (i.e., cells with small fractional area) (Figs. 10c,d). Similar performance differences were noted between the continental and maritime style cells when looking further into the subset of cases located specifically over the ocean. Analysis of the hazardous cells not detected by the algorithms reveals significantly more variability among the algorithm detection values for cells classified as continental. This observation coupled with the poorer performance in measured FAR could be due to a combination of factors: 1) the time allowance (15 min) used during the TRMM and GOES grid matching where the smaller cells may have rapidly developed (decayed) to (from) a hazardous level as viewed by the TRMM satellite but not in the GOES satellite-based products, and 2) the reflectivity sampling of the PR (with its less-than-ideal ~ 4 -km horizontal resolution) did not capture the small reflectivity cores, hence reducing the number of "hazardous" cells identified and increasing the opportunity for false alarms.

Regarding comparison of detection performance between the day and nighttime cells (Figs. 10e,f), the CTOP and GCD algorithms perform similarly with re-

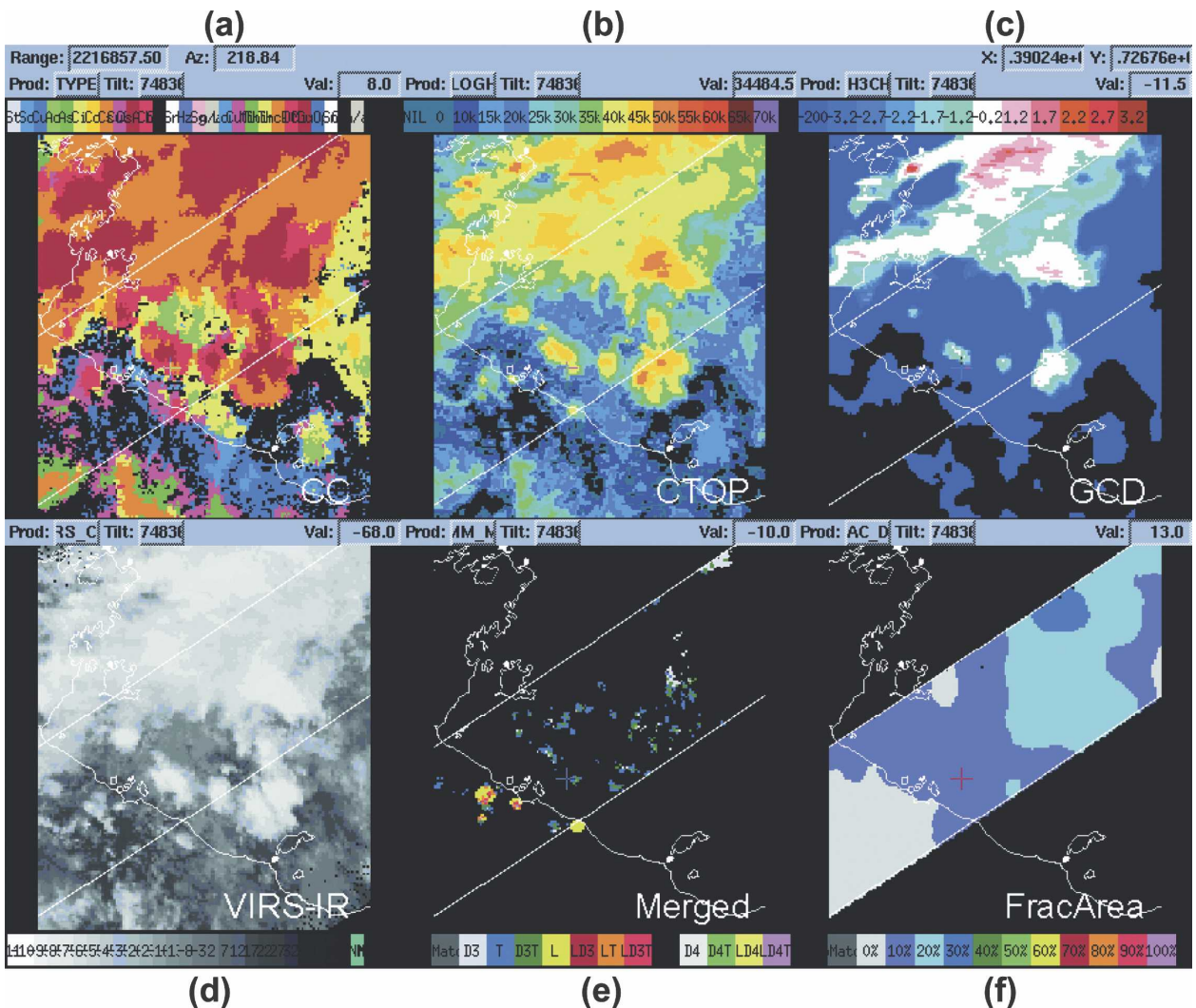


FIG. 8. Illustration of an analysis display used to evaluate the (a)–(c) convection diagnostic products with (d)–(f) the TRMM product data observed in the Gulf of Carpentaria (upper right of each image) and northern Australia (lower and left portion of each image) on 18 Mar 2004 at 0538 UTC. The TRMM merged data in (e) were used to record single or combined observations of lightning (L), reflectivity values above 30 (D3) and 40 (D4) dBZ at 5-km altitude, or convective rain (T), and the fractional area of radar reflectivity ≥ 20 dBZ in (f) was used to distinguish between a maritime or continental regime.

spect to each other. The CTOP CSI for daytime cells was 7% higher than for nighttime cells. The CC algorithm shows an improved detection rate, a distinct increase in the FAR, and a 14% reduction in CSI for nighttime cells. The increase in CC POD (7%) and FAR (24%) is likely an artifact of the aggressive algorithm behavior at night and can probably be attributed to the loss of the satellite visible channel. Lack of any higher-resolution data (visible channel is 1 km versus 4 km for infrared channels) and use of larger sample boxes can lead to misclassifications at night. The bias toward deep convection needs further study to quantify the difference in performance.

Figure 11 contains frequency distribution plots of the output values issued by each algorithm for all hazardous cells identified. The dashed vertical lines in the CTOP and GCD plots represent the current algorithm threshold used to diagnose deep convection. All values of cloud-top height (Fig. 11a) to the right (left) of the vertical line denote algorithm hits (misses). The abundance of missed detections in the 30–39-kft (9.1–11.9-km) range suggests the need to lower the threshold to catch this subset of cases at the expense of potentially increasing the FAR. The three dashed lines in the CC plots (Figs. 11b,c) represent correct identifications of cloud type for deep convection for daytime (Fig. 11b)

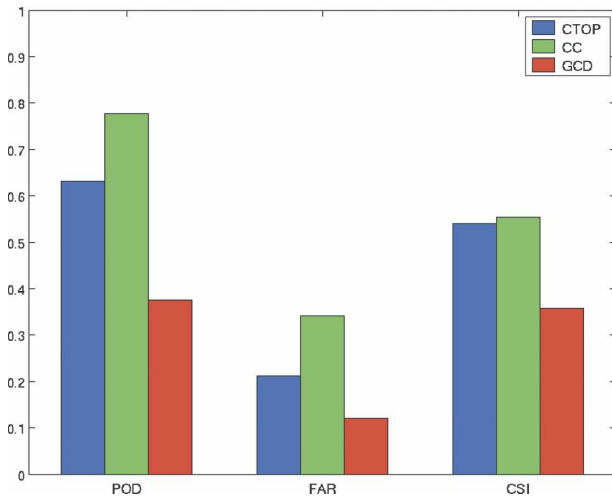


FIG. 9. Histogram of the performance statistics for the CTOP (blue), CC (green), and GCD (red) algorithms in the third intercomparison. A total of 649 cells were identified in the TRMM data as possibly hazardous. The scoring metrics are defined as the POD, FAR, and CSI.

and nighttime (Fig. 11c) classifications. The misclassification of the daytime cells all seem to fall into cloud categories that have some vertical development [i.e., cumulus (Cu) and cumulus congestus (Cg)] or reside at high altitudes [i.e., cirrus (Ci) and cirrostratus (Cs)]. Note that the algorithm does not misdiagnose low- or midlevel cloud types. Among the few cells missed at night, most were identified in the mixed (Mx) type category (thin high clouds over low clouds), which may be due to the similarity in texture and/or pixel value variability within a given sample (between DC and Mx types). In the GCD detection plot (Fig. 11d), satellite channel temperature differences to the right (left) of the dashed vertical line correspond to hits (misses). The extension of temperature differences to -25°C is not well understood at present.

Performance statistics among the three algorithm products in their ability to detect the strongest hazardous cells, namely, those that contained lightning (105), over both land and ocean combined, are presented in Table 3. The probability of missed (POM) detections is included in the table and represents the ratio of the number of TRW not detected to the total number of TRW identified by the TRMM LIS (i.e., $1 - \text{POD}$). FAR and CSI do not apply here because the algorithms should not be penalized for identifying deep, potentially hazardous convection that do not contain lightning (CWL). The CC algorithm obtained the highest POD (84%) overall followed by the CTOP (67%) and the GCD (43%). These POD rates are 4%–7% higher for the subset of hazardous cells that contained light-

ning compared to the POD for the hazardous cells that exhibited single or combined signature of reflectivity, convective rain, or lightning (Figs. 10a,b). It is particularly noteworthy that the largest values for POD are achieved when lightning alone is used as a criterion for “hazardous cell.” Among the TRW missed by the algorithms, more than 50% were located outside the PR swath where no reflectivity information was available for further study. However, consistent with the product value distribution charts shown for all hazardous cells (Fig. 11), the product values were not that far off from current algorithm thresholds for this subset of cells.

The reflectivity profiles (defined in section 5a) for various subsets of categories were also studied. Figure 12 contains a plot of the mean reflectivity profiles (average of linear Z values at each altitude) for all TRW identified by the LIS subdivided into classes of ocean–continental (blue), ocean–maritime (green), land–continental (red), and land–maritime (yellow). As expected, the mean land profiles are stronger than the oceanic profiles (Petersen and Rutledge 2001; Cecil et al. 2005). Of greater importance is the fact that the maritime profiles are stronger than the continental profiles, especially for the cells over the ocean. This comparison is consistent with the differences observed between the mean flash rate of the maritime ($1.9 \text{ flash min}^{-1}$) and continental cells ($1.4 \text{ flashes min}^{-1}$). However, given the limited profile sample size, these results may not be representative of the average profile structure among each category.

The mean profile of all cells presumed to be hazardous over the ocean (following the criteria described earlier) was then compared and are shown in Fig. 13. Below 14 km, the maritime profile is again stronger at all altitudes especially from the near-surface up to the 6-km altitude. A t test was applied to the data and the results indicate a statistical significance between the two profiles at all but a few altitude levels above 11 km using a significance level of 0.05. The evidence of relative maxima at 4.5 km in each profile is characteristic of a brightband signature from nonhazardous cells. The inclusion of nonconvective cells can be attributed to the conservative thresholds used for “hazardous cell.” The selection of attenuation-uncorrected profiles in this study may impact the reflectivity in the lower portion of the profile, but should not affect the general ordering of the profiles in Figs. 12 and 13.

6. Discussion and interpretation

Some consistent results emerge across the three satellite intercomparisons. The good news in the operational context is that the majority of TRMM-verified

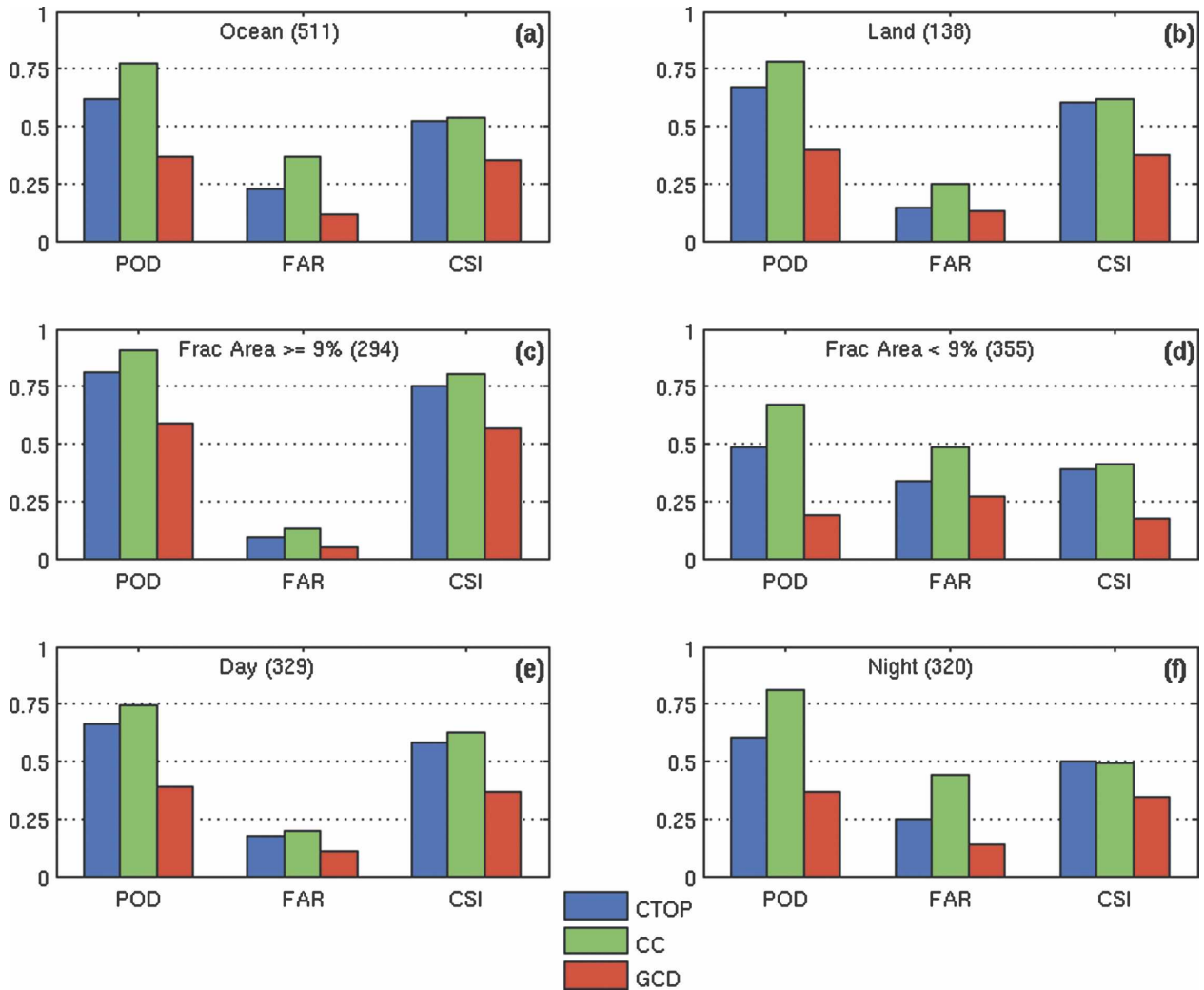


FIG. 10. Performance statistics among the three algorithms in their ability to detect hazardous cells in the third intercomparison distinguished on whether the cell was located over the (a) ocean or (b) land, exhibited (c) large and (d) small fractional area of radar reflectivity ≥ 20 dBZ at 5-km altitude, and observed (e) during the day or (f) at night. The scoring metrics are defined as the POD, FAR, and CSI.

hazardous cells are correctly identified by the diagnostic algorithms. (This is to say that the POD values in Tables 1, 2, and 3 and Figs. 9 and 10 can exceed 90% when observed lightning is used as the criterion for “hazardous” status). Perfect algorithm detection in the presence of both imperfect algorithms and imperfect verification cannot be expected. The horizontal resolution of the TRMM PR can smear narrow reflectivity cores, and the time skew between the geostationary satellite products and the TRMM observations can allow storm evolution to negatively impact the verification process.

The not-so-good news in the operational context is that a substantial number of convective cells not verified as TRW, or not deemed hazardous by other crite-

ria, can masquerade (or “false alarm”) as hazardous cells. (This is to say that the FAR values are substantial in the cases that compose Tables 1 and 2 and Figs. 9 and 10, and occasionally exceed 40%). These high FAR results are also manifest at a larger scale in comparisons of global maps of TRW and CWL. The oceanic regions are relatively richer in the latter category (see also Williams 2005 for a literature summary of similar results).

This unfavorable result exposes a fundamental limitation in the use of satellite visible and IR observations (in isolation) for identifying hazardous weather. The origin of this problem has been traced to a simple cause: a large number of oceanic cumulonimbus clouds attain high altitude but lack a strong updraft (and attendant radar reflectivity aloft and associated lightning activ-

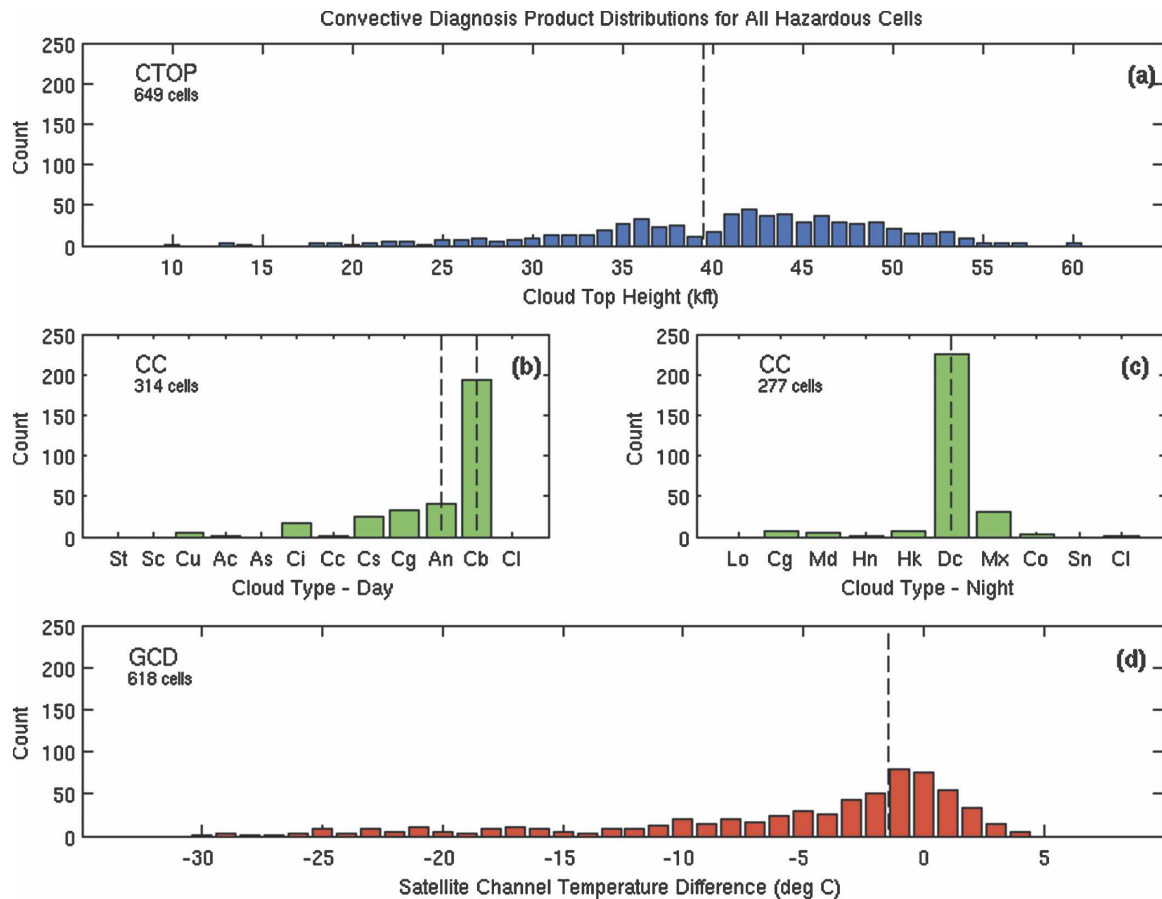


FIG. 11. Distribution histograms of the detections produced by the (a) CTOP, CC for (b) daytime and (c) nighttime, and (d) GCD algorithms for all hazardous cells identified in the third intercomparison. Detections to the right of the dashed vertical lines in the CTOP and GCD plots represent correct diagnosis of deep, potentially hazardous convection. The dashed lines in both CC plots represent correct cloud category identifications of hazardous convection. The An, Cb, and DC cloud categories correspond to cirrostratus cloud associated with deep convection, cumulonimbus cloud, and deep convection at night, respectively. Fewer cells were evaluated for the CC and GCD products because of algorithm data availability.

ity). This result stands in marked contrast with the large body of evidence for continental convection, showing that clouds attaining tropopause heights are almost invariably producing lightning and presenting a legitimate hazard to aviation. In extreme continental situations, the tendency for severe weather hazards over land to increase with cloud height is well established (Darrah 1978). Furthermore, the tendency for the lightning flash rate to increase strongly with cloud height is also well established (Williams 1985, 2001; Ushio et al. 2005). This situation invites another look at the differences between continental and oceanic convection for further understanding. Given the restricted latitude limits for verification by the TRMM satellite ($\pm 35^\circ$), most of the discussion herein pertains to lower latitudes, where deep convection attains the greatest altitude in general.

A useful starting point for this discussion is a consid-

eration of land–ocean contrasts in relevant cloud/thermodynamic parameters in Table 4. These rough estimates are extracted from the literature on convective available potential energy (CAPE; Williams and Renno

TABLE 3. Performance statistics among the algorithms in their ability to identify the strongest hazardous cells, i.e., those cells that contained lightning, observed over land and ocean (105) during the third intercomparison. The scoring metrics from left to right are as follows: Hits (number correct), misses (failure to detect), bad (product not available), POD, and POM detections.

| Hazardous cells containing lightning (105) | | | | | |
|--|------|--------|-----|------|------|
| Satellite product | Hits | Misses | Bad | POD | POM |
| CC | 80 | 15 | 10 | 0.84 | 0.16 |
| GCD | 43 | 56 | 6 | 0.43 | 0.57 |
| CTOP ≥ 40 kft | 70 | 35 | 0 | 0.67 | 0.33 |
| CTOP ≥ 35 kft | 86 | 19 | 0 | 0.82 | 0.18 |
| CTOP ≥ 30 kft | 97 | 8 | 0 | 0.92 | 0.08 |

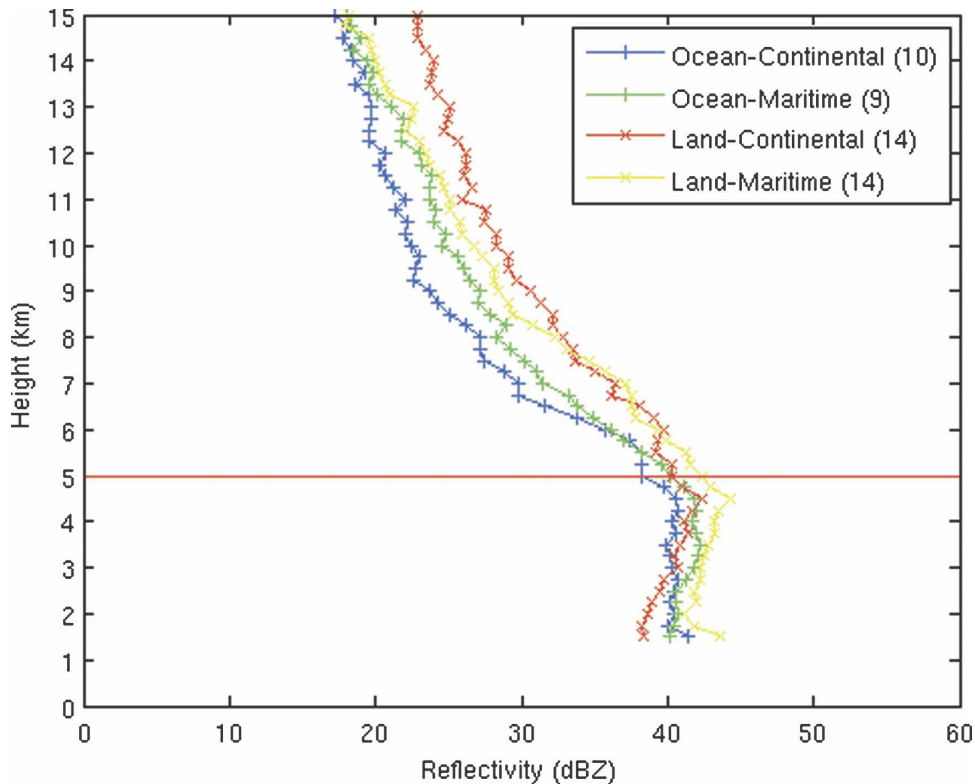


FIG. 12. Profiles of mean reflectivity vs height for all the cells that contained lightning distinguished on the basis of the fractional area test. Profiles are subdivided into categories of cells over the ocean that exhibited continental (blue) or maritime (green) characteristics and over land (red and yellow, respectively).

1993; Lucas et al. 1994; Williams and Stanfill 2002; Zipser 2003), level of neutral buoyancy (LNB; Williams and Renno 1993), cloud heights (Hendon and Woodberry 1993; Anyamba et al. 2000; this study), updraft speed (Zipser and LeMone 1980; Williams and Stanfill 2002), updraft width (Williams and Stanfill 2002), cloud-base height (Lucas et al. 1994; Betts 1997; Williams and Stanfill 2002; Williams et al. 2005), and concentration of cloud condensation nuclei (CCN; Williams et al. 2002).

The traditional explanation for the contrast in observed updraft speed between land and ocean is based on parcel theory and CAPE. The ocean surface is mobile and is characterized by large heat capacity, both of which serve to suppress surface temperature rise by incident sunlight and the strong destabilization of surface air parcels. However, more recent scrutiny has shown that the contrast in CAPE between land and ocean is not adequate to explain the contrast in updraft speeds (Williams and Renno 1993; Lucas et al. 1994; Williams and Stanfill 2002; Zipser 2003). The maximum wet-bulb potential temperatures are larger over land, but so are the temperatures at midlevels of the atmo-

sphere (Williams and Renno 1993). So both the temperature sounding and the wet-bulb adiabats are displaced slightly leftward for the oceans, with relatively little change (Table 4) in the LNB, which is the parcel-theory indicator of cloud-top height. This is to say that the land and the ocean are “convectively adjusted” in some sense. On this basis, one does not expect large differences in cloud height between land and ocean, regardless of the contrast in updraft speed (Table 4).

Other research work (Barnes 2001; Petersen et al. 2006) has suggested that differences in the vertical distribution of cloud buoyancy (i.e., the “shape of the CAPE”) may explain the observed contrast in updraft speed between land and ocean (Table 4). The updraft speeds that are computed, however, are systematically larger than those observed.

Williams and Stanfill (2002) and Williams et al. (2005) have presented evidence that departures from parcel theory are essential in explaining the contrast in updraft speed between land and ocean. Larger rising parcels are expected over land with higher cloud-base heights and thicker boundary layer reservoirs of unstable air (Williams et al. 2005). These larger parcels

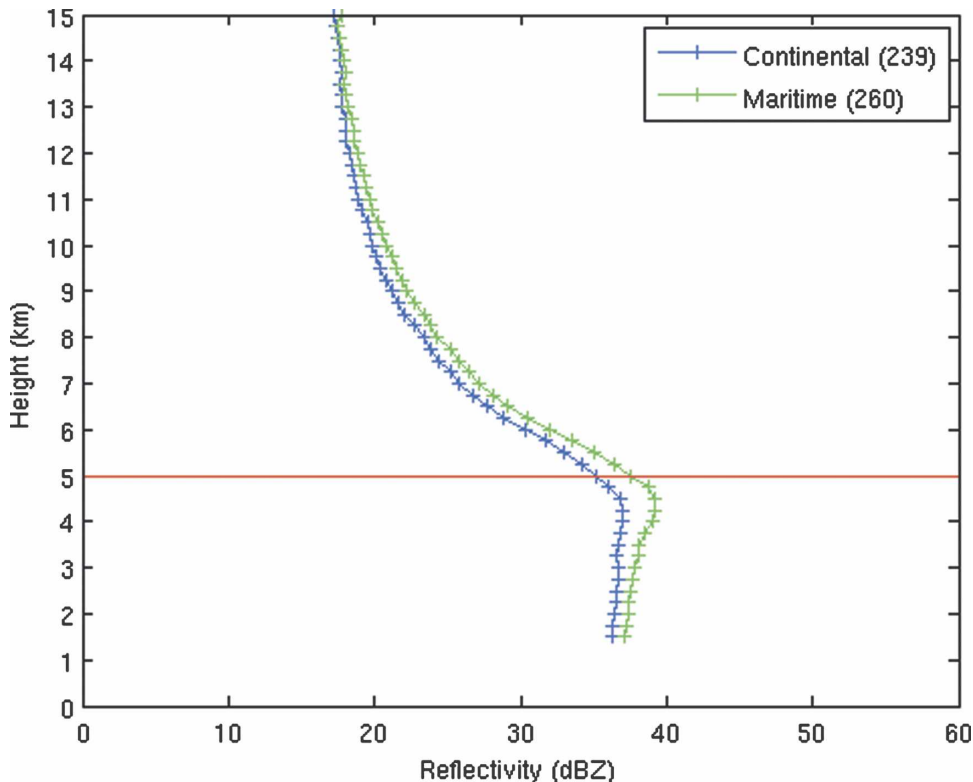


FIG. 13. Profiles of mean reflectivity vs height among all the oceanic cells presumed hazardous and distinguished on the basis of the fractional area test. Note the maritime cells exhibited the strongest mean profile, particularly below 6 km.

are more immune to mixing and more likely to attain ascent speeds in line with parcel-theory predictions (Williams and Stanfill 2002). Observational differences in both cloud-base height and updraft width (Table 4) are substantial between land and ocean, and can account for the large contrast in updraft speed.

The aerosol hypothesis (Williams et al. 2002; Rosenfeld and Woodley 2003; Khain et al. 2005) presents a different explanation for the contrast in updraft strength between land and ocean, based on the early formation of “warm rain” and the consequent superadiabatic loading of the updraft parcel (Khain et al. 2005). This idea is not strongly supported by the vertical profiles of radar reflectivity in Fig. 12, showing little tendency for stronger profiles at lower levels in the more maritime cases. More importantly, the aerosol hypothesis does not account for the systematic differences in updraft width between land and ocean (Williams and Stanfill 2002 and Table 4) that we link with differential departures from parcel theory.

The new comparative results over the oceans using fractional area as a parameter in the third satellite intercomparison (Fig. 13) can likewise be interpreted in the context of a departure from parcel theory. Here it

was shown that the vertical profiles of radar reflectivity were stronger, on average, in the cases exhibiting large fractional area. This finding ran contrary to our initial expectations concerning continental and maritime characteristics and our expectations based on parcel theory. Namely, the underlying ocean surface would experience stronger heating in the more exposed surface of the low fractional area case, with corresponding greater instability, stronger updraft, and stronger vertical reflectivity profile.

TABLE 4. Rough estimates of the approximate contrast in relevant cloud/thermodynamic parameters between land and ocean convection. All land values exceed ocean values.

| Land–ocean contrast in relevant parameters | |
|--|---------------------------------|
| Quantity | Approximate land–ocean contrast |
| CAPE | +10% |
| LNB | +10% |
| Cloud heights | +10% |
| Updraft speeds | +×2–5 |
| Updraft widths | +×2 |
| Cloud-base height | +×2 or more |
| CCN | +×10 |

We do not expect a difference in cloud-base height for the low and high fractional area cases, as they are both oceanic cases for which the surface relative humidity is close to 80%. But if departures from parcel theory are considered [noted initially in the Thunderstorm Project (Byers and Braham 1949) results], it can be expected that cases with low fractional area will be more susceptible to entrainment of drier environmental air (and subsequent dilution) than the high fractional area cases that are more likely surrounded with saturated air. We are not aware that comparisons of this kind have been previously undertaken. It is important to add that since we lack comparisons of CAPE between the low and the high fractional area cases, we cannot rule out differences in instability in accounting for the differences in the reflectivity profiles.

The broad conclusion in considerations of both the observations in this study and the work documented in the literature (Williams and Stanfill 2002; Zipser 2003) is that departures from parcel theory are essential in accounting for the weak updrafts in deep oceanic clouds. An important caveat from an operational standpoint is the possibility that deep oceanic cumulonimbi without lightning and without enhanced radar reflectivity aloft will present a significant hazard to aviation. In any case, different criteria need to be applied operationally in the interpretation of hazardous conditions in oceanic and continental clouds.

7. Conclusions

Despite shortcomings in verification due to horizontal resolution in the TRMM PR sampling and modest (~15 min) time skew among the datasets, the three satellite algorithms have shown an ability to detect a large fraction of the most hazardous cells—those that contained lightning. However, each algorithm also has a tendency to overestimate the presence of hazardous oceanic convection, a situation that could be improved through adjustments in thresholds for hazard.

Results from this study illustrate a fundamental limitation in using satellite visible and infrared information alone to make proper inferences about the internal characteristics of deep convective cells over the ocean, specifically the hazards associated with updraft strength and turbulence. Comparisons in the relevant thermodynamic parameters between land and ocean are discussed and do not explain on the basis of parcel theory alone the differences in updraft strength for clouds attaining similar cloud-top heights. A fractional area test of the spatial reflectivity observed in the mixed-phase region of the cloud was introduced in the third intercomparison to distinguish hazardous cells exhibiting

“maritime” and “continental” characteristics. Contrary to our expectations and a departure from parcel theory, the vertical reflectivity structure within the maritime cells was stronger on average than in the continental cells. It is believed that entrainment of dry air and the subsequent erosion of the cloudy area is occurring in cells exhibiting low fractional area, whereas the high fractional area cells are surrounded by saturated maritime air and hence protected. Further observations of oceanic convection are needed to verify this interpretation of results.

Acknowledgments. This work was funded by the Aviation Weather Research Program (AWRP) of the Federal Aviation Administration (FAA). We thank Gloria Kulesa, Pete Kirchoffer, and Warren Fellner for their support. The views expressed are those of the authors and do not necessarily represent the official policy or position of the FAA.

The TRMM visible, IR, and radar data used for verification in these intercomparisons were provided by the Goddard Distributed Active Archive Center (DAAC) and with much assistance from the TRMM Science Data and Information System (TSDIS) helpdesk. Data from the TRMM Lightning Imaging Sensor were provided by the Global Hydrology Research Center (GHRC), NASA Marshall Space Flight Center (MSFC).

REFERENCES

- Anyamba, E., E. Williams, J. Susskind, A. Fraser-Smith, and M. Fullekrug, 2000: The manifestation of the Madden-Julian oscillation in global deep convection and in Schumann resonance intensity. *J. Atmos. Sci.*, **57**, 1029–1044.
- Awaka, J., T. Iguchi, and K. Okamoto, 1998: Early results on rain type classification by the Tropical Rainfall Measuring Mission (TRMM) Precipitation Radar. *Proc. Eighth URSI Commission F Open Symp.*, Aveiro, Portugal, Union Radio-Scientifique Internationale, 143–146.
- Baker, M. B., H. J. Christian, and J. Latham, 1995: A computational study of the relationships linking lightning frequency and other thundercloud parameters. *Quart. J. Roy. Meteor. Soc.*, **121**, 1525–1548.
- Bankert, R. L., and D. W. Aha, 1996: Improvement to a neural network cloud classifier. *J. Appl. Meteor.*, **35**, 2036–2039.
- Barnes, G., 2001: Severe local storms in the tropics. *Severe Convective Storms, Meteor. Monogr.*, No. 50, Amer. Meteor. Soc., 359–432.
- Betts, A. K., 1997: The parameterization of deep convection. *The Physics of Parameterization of Moist Atmospheric Convection*, R. K. Smith, Ed., Kluwer Academic, 255–279.
- Boccippio, D. J., 2002: Lightning scaling relations revisited. *J. Atmos. Sci.*, **59**, 1086–1104.
- , K. Driscoll, J. Hall, and D. Buechler, 1998: LIS/OTD software guide. Global Hydrology and Climate Center, NASA Marshall Space Flight Center, 142 pp.

- Byers, H. R., and R. R. Braham, 1949: *The Thunderstorm*. U.S. Government Printing Office, 287 pp.
- Cecil, D. J., S. J. Goodman, D. J. Boccippio, E. J. Zipser, and S. W. Nesbitt, 2005: Three Years of TRMM precipitation features. Part I: Radar, radiometric, and lightning characteristics. *Mon. Wea. Rev.*, **133**, 543–566.
- Christian, H. J., and Coauthors, 2003: Global frequency and distribution of lightning as observed from space by the Optical Transient Detector. *J. Geophys. Res.*, **108**, 4005, doi:10.1029/2002JD002347.
- Darrah, R. P., 1978: On the relationship of severe weather to radar tops. *Mon. Wea. Rev.*, **106**, 1332–1339.
- Hendon, H. H., and K. Woodberry, 1993: The diurnal cycle of tropical convection. *J. Geophys. Res.*, **98**, 16 623–16 637.
- Herzogh, P. H., E. R. Williams, T. A. Lindholm, F. R. Mosher, C. Kessinger, R. Sharman, J. D. Hawkins, and D. B. Johnson, 2002: Development of automated aviation weather products for oceanic/remote regions: Scientific and practical challenges, research strategies, and first steps. Preprints, *10th Conf. on Aviation, Range, and Aerospace Meteorology*, Portland, OR, Amer. Meteor. Soc., 57–60.
- Jorgensen, D. P., and M. A. LeMone, 1989: Vertical velocity characteristics of oceanic convection. *J. Atmos. Sci.*, **46**, 621–640.
- Khain, A., D. Rosenfeld, and A. Pokrovsky, 2005: Aerosol impact on the dynamics and microphysics of deep convective clouds. *Quart. J. Roy. Meteor. Soc.*, **131**, 1–25.
- Kummerow, C., W. Barnes, T. Kozu, J. Shiue, and J. Simpson, 1998: The Tropical Rainfall Measuring Mission (TRMM) sensor package. *J. Atmos. Oceanic Technol.*, **15**, 809–817.
- Larsen, H. R., and E. J. Stansbury, 1974: Association of lightning flashes with precipitation cores extending to 7 km. *J. Atmos. Terr. Phys.*, **36**, 1547–1553.
- LeMone, M. A., and E. J. Zipser, 1980: Cumulonimbus vertical velocity events in GATE. Part 1: Diameter, intensity and mass flux. *J. Atmos. Sci.*, **37**, 2444–2457.
- Lucas, L., E. J. Zipser, and M. A. LeMone, 1994: Convective Available Potential Energy in the environment of oceanic and continental clouds: Corrections and comments. *J. Atmos. Sci.*, **51**, 3829–3830.
- Mahoney, J., B. Brown, C. Mueller, and J. Hart, 2000: Convective intercomparison exercise: Baseline statistical results. Preprints, *Ninth Conf. on Aviation, Range, and Aerospace Meteorology*, Orlando, FL, Amer. Meteor. Soc., 403–408.
- Marshall, J. S., and S. Radhakant, 1978: Radar precipitation maps as lightning indicators. *J. Appl. Meteor.*, **17**, 206–212.
- Martin, D. W., R. A. Kohrs, F. R. Mosher, C. M. Medaglia, and C. Adamo, 2008: Over-ocean validation of the Global Convective Diagnostic. *J. Appl. Meteor. Climatol.*, in press.
- Mosher, F., 2002: Detection of deep convection around the globe. Preprints, *10th Conf. on Aviation, Range, and Aerospace Meteorology*, Portland, OR, Amer. Meteor. Soc., 289–292.
- Nesbitt, S. W., E. J. Zipser, and D. J. Cecil, 2000: A census of precipitation features in the tropics using TRMM: Radar, ice scattering, and lightning observations. *J. Climate*, **13**, 4087–4106.
- , R. Cifelli, and S. A. Rutledge, 2006: Storm morphology and rainfall characteristics of TRMM precipitation features. *Mon. Wea. Rev.*, **134**, 2702–2721.
- Petersen, W. A., and S. A. Rutledge, 2001: Regional variability in tropical convection: Observations from TRMM. *J. Climate*, **14**, 3566–3586.
- , —, and R. E. Orville, 1996: Cloud-to-ground lightning observations from TOGA COARE: Selected results and lightning location algorithms. *Mon. Wea. Rev.*, **124**, 602–620.
- , —, R. C. Cifelli, B. S. Ferrier, and B. F. Smull, 1999: Shipborne dual-Doppler operations during TOGA COARE: Integrated observations of storm kinematics and electrification. *Bull. Amer. Meteor. Soc.*, **80**, 81–97.
- , H. J. Christian, and S. A. Rutledge, 2005: TRMM observations of a relationship between ice water content and lightning. *Geophys. Res. Lett.*, **32**, L14819, doi:10.1029/2005GL023236.
- , R. Fu, M. Chen, and R. Blakeslee, 2006: Intraseasonal forcing of convection and lightning activity in the southern Amazon as a function of cross-equatorial flow. *J. Climate*, **19**, 3180–3196.
- Pinsky, M., and A. Khain, 2002: Effects of in-cloud nucleation and turbulence on drop spectrum formation in cumulus clouds. *Quart. J. Roy. Meteor. Soc.*, **128**, 501–533.
- Rosenfeld, D., and W. L. Woodley, 2003: Closing the 50-year circle: From cloud seeding to space and back to climate change through precipitation physics. *Cloud Systems, Hurricanes and Tropical Rainfall Measuring Mission (TRMM)*, Meteor. Monogr., No. 51, Amer. Meteor. Soc., 59–80.
- Shackford, C. R., 1960: Radar indications of a precipitation-lightning relationship in New England thunderstorms. *J. Atmos. Sci.*, **17**, 15–19.
- Steiner, M., R. A. Houze Jr., and S. E. Yuter, 1995: Climatological characterization of three-dimensional storm structure from operational radar and rain gauge data. *J. Appl. Meteor.*, **34**, 1978–2007.
- Tag, P. M., R. L. Bankert, and L. R. Brody, 2000: An AVHRR multiple cloud-type classification package. *J. Appl. Meteor.*, **39**, 125–134.
- Takahashi, T., 1978: Electrical properties of oceanic tropical clouds at Ponape, Micronesia. *Mon. Wea. Rev.*, **106**, 1598–1612.
- Toracinta, E. R., D. J. Cecil, E. J. Zipser, and S. W. Nesbitt, 2002: Radar, passive microwave, and lightning characteristics of precipitating systems in the tropics. *Mon. Wea. Rev.*, **130**, 802–824.
- Ushio, T., S. Sakurai, T. Mega, K. Okamoto, and Z. Kawasaki, 2005: On the relationship between vertical profile of radar reflectivity and lightning flash rate observed by the TRMM/PR and LIS. *J. Atmos. Electr.*, **25**, 47–53.
- Williams, E. R., 1985: Large-scale charge separation in thunderclouds. *J. Geophys. Res.*, **90**, 6013–6025.
- , 2001: The electrification of severe storms. *Severe Convective Storms*, Meteor. Monogr., No. 50, Amer. Meteor. Soc., 527–561.
- , 2005: Lightning and climate: A review. *Atmos. Res.*, **76**, 272–287.
- , and R. M. Lhermitte, 1983: Radar tests of the precipitation hypothesis for thunderstorm electrification. *J. Geophys. Res.*, **88**, 10 984–10 992.
- , and N. O. Renno, 1993: An analysis of the conditional instability of the tropical atmosphere. *Mon. Wea. Rev.*, **121**, 21–36.
- , and S. Stanfill, 2002: The physical origin of the land-ocean contrast in lightning activity. *C. R. Phys.*, **3**, 1277–1292.
- , S. A. Rutledge, S. G. Geotis, N. Renno, E. Rasmussen, and T. Rickenbach, 1992: A radar and electrical study of tropical “hot towers.” *J. Atmos. Sci.*, **49**, 1386–1395.

- , K. Rothkin, D. Stevenson, and D. Boccippio, 2000: Global lightning variations caused by changes in thunderstorm flash rate and by changes in the number of thunderstorms. *J. Appl. Meteor.*, **39**, 2223–2230.
- , and Coauthors, 2002: Contrasting convective regimes over the Amazon: Implications for cloud electrification. *J. Geophys. Res.*, **107**, 8082, doi:10.1029/2001JD000380.
- , V. Mushtak, D. Rosenfeld, S. Goodman, and D. Boccippio, 2005: Thermodynamic conditions favorable to superlative thunderstorm updraft, mixed phase microphysics and lightning flash rate. *Atmos. Res.*, **76**, 288–306.
- Zipser, E. J., 2003: Some views on “hot towers” after 50 years of tropical field programs and two years of TRMM data. *Cloud Systems, Hurricanes, and the Tropical Rainfall Measuring System (TRMM)*, *Meteor. Monogr.*, No. 51, Amer. Meteor. Soc., 49–58.
- , and M. A. LeMone, 1980: Cumulonimbus vertical velocity events in GATE. Part II: Synthesis and model core structure. *J. Atmos. Sci.*, **37**, 2458–2469.
- , and K. R. Lutz, 1994: The vertical profile of radar reflectivity in convective cells: A strong indicator of storm intensity and lightning probability? *Mon. Wea. Rev.*, **122**, 1751–1759.